ARCHIVES
of
FOUNDRY ENGINEERING

10.24425/afe.2026.158023

Published quarterly as the organ of the Foundry Commission of the Polish Academy of Sciences

ISSN (2299-2944)
Volume 2026
Issue 3/2026

95 – 109
12/3

Investigating the Effect of Diameter-to-Height Ratio of the Starter Block on the Microstructure and Crystallographic Orientation of CMSX-4 Single Crystal

Ali Jadidi *, Mahdi Ezheiyyan, Seyed Mahdi Abbasi, Masumeh Seifollahi
Malek Ashtar University of Technology, Iran
* Corresponding author. E-mail address: alijdidi13@gmail.com

Received 07.11.2025; accepted in revised form 20.08.2026; available online 23.09.2026

Abstract

The present study investigates the effect of starter-block diameter-to-height (D/H) ratio on grain selection, crystallographic orientation, solidification microstructure, and γ′ precipitate morphology in directionally solidified CMSX-4 single-crystal castings. Starter blocks with D/H ratios of 0.3, 0.5, and 0.7 were produced using a Bridgman-type directional solidification process at a withdrawal rate of 9 mm/min. Laue X-ray diffraction, optical and scanning electron microscopy, image analysis, and ProCAST numerical simulations were employed to evaluate the crystallographic and microstructural characteristics of the castings. All investigated castings exhibited single-crystal growth in the examined cross-sections. The measured misorientation angles from the preferred crystallographic orientation were 6.3°, 21.7°, and 3.3° for D/H ratios of 0.3, 0.5, and 0.7, respectively, indicating a non-monotonic dependence on starter-block geometry. The relatively large misorientation at D/H = 0.5 was associated with altered local thermal conditions, increased sensitivity to lateral heat extraction, and possible destabilization of the solid-liquid interface. Stray grains were observed in the D/H = 0.3 and 0.5 castings but were not detected in the D/H = 0.7 casting. The simulations indicated that the solidification front advanced into the colder furnace region beyond the heat baffle, where the local thermal gradient decreased substantially and could promote wall-associated stray-grain nucleation. Nevertheless, the survival of these grains was also influenced by dendrite alignment and competitive growth. The measured primary and secondary dendrite arm spacings showed substantial overlap, and no statistically conclusive relationship with the starter-block D/H ratio was identified. Grain-count analysis demonstrated a progressive reduction in grain density with increasing distance from the chill plate. Both D/H ratio and distance had statistically significant main effects, whereas their interaction was not significant. Image analysis of γ′-related regions in the primary dendrite cores showed comparable area fractions and broadly similar shape descriptors for D/H ratios of 0.3 and 0.5, while the lower feature count at D/H = 0.5 suggested a relatively coarser or more interconnected morphology. Overall, the results show that starter-block geometry primarily affects local thermal conditions and competitive grain selection, thereby influencing crystallographic quality and stray-grain formation, whereas its effect on average dendrite spacing and local γ′ morphology was comparatively limited within the investigated conditions.

Keywords: Single-crystal superalloy, Grain selector, Starter block, Dendrite spacing; γ′ precipitates, Stray grains

© The Author(s) 2026. Open Access. This article is licensed under a Creative Commons Attribution 4.0 International License (http://creativecommons.org/licenses/by/4.0/), which permits use, sharing, adaptation, distribution and reproduction in any medium or format, as long as you give appropriate credit to the original author(s) and the source, provide a link to the Creative Commons licence, and indicate if changes were made.

1. Introduction

Nickel-based single crystal superalloys are widely utilized in the manufacture of aerospace and land-based turbine blades due to their outstanding high-temperature properties [1]. The grain selector system, initially developed by Pratt & Whitney, plays a crucial role in optimizing performance. The greatest creep life of a single crystal component is achieved when the deviation from the [001] orientation is minimized. For turbine blades, this deviation must be kept within 10˚[2].

According to Meng et al. [3], a grain selector height of 20 - 30 mm, with a pitch of 30 mm and one full turn, was sufficient for effective grain selection. Additionally, Wang et al. [4] found that reducing the diameter-to-height ratio of the starter block decrease deviation from the preferred crystal orientation. Carter et al. [5] determined the optimal height and diameter for the starter block in CMSX-4 superalloy as 25 mm and 20 mm, respectively, corresponding to a diameter-to-height ratio of 0.8. Furthermore, Wang et al. [1] reported that to achieve a single crystal, the starter block height must be at least 26 mm. Moreover, increasing the height-to-diameter ratio of the starter block reduced the deviation of the final single crystal from the preferred orientation, with a diameter-to-height ratio of 0.5 being ideal.

Sadeghi et al. [6] determined that achieving single crystal casting with minimal deviation from the preferred crystal orientation required a diameter-to-height ratio of the starter block to be less than 0.6. In the grain selection process, the height of the starter block was more influential than its diameter, and a starter block height of 35 mm was adequate to ensure effective casting while maintaining grain selection efficiency, i.e., minimizing the number of competing grains. Therefore, additional height was unnecessary. They found that diameter-to-height ratios of 2.3 and 1.2 correspond to deviations of 12.94˚ and 10.61˚ from the preferred orientation, respectively. Both increasing the diameter and height of the starter block reduced deviation from the preferred orientation, with height having a more significant effect. Sadeghi et al. [6] also suggested that the optimal parameters for the grain selector were an angle between 30 - 45˚ and a diameter of 3 mm.

According to Zhu et al. [7], the optimal height of the starter block was 10 - 30 mm. Heights below 10 mm did not achieve stable growth conditions, while increasing the height beyond 30 mm yielded no additional benefits and only escalated production costs. Furthermore, to ensure an adequate number of grains were introduced into the grain selector, the diameter of the starter block had to be carefully controlled within an optimal range. The recommended diameter was between 10 and 20 mm, as diameters exceeding 20 mm gave unnecessary cost increases without improving grain selection efficiency or reducing the number of grains per unit area. Additionally, a larger diameter in the starter block can further refine the crystal orientation, minimizing deviations from the preferred [001] crystal orientation. Moreover, as the height of the starter block increased, the average deviation of the formed grains from the preferred [001] orientation diminished. Pan et al. [8] investigated the DD6 superalloy and found that competitive grain growth within the starter block led to the preferential elimination of grains with greater deviations from the desired crystal orientation. Consequently, the grains that were selected exhibited reduced angular deviations from the preferred orientation. Similarly, Gao et al. [9] found that for the DD3 superalloy, as the distance from the chill plate increased, the proportion of grains with deviations of less than 10˚ from the preferred crystal orientation increased. Meng et al. [2] reported increased height of the starter block decreased grain count per unit area and a reduction in the final grain's deviation from the preferred crystal orientation.

Jiang et al. [10] showed that grain competition during growth of IC6SX single crystal was affected solely by dendritic orientations, rather than grain size. Typically, the grain with the least deviation from the preferred orientation prevails in these competitions. Most sources gave optimal heights for the starter block as 10 - 40 mm [1,4,5,7,11-14]. For single crystal superalloy CMSX-4, the optimal height for the starter block was 20 - 40 mm [1,4,11,13]. Another critical parameter is the diameter of the starter block, which, with height, defines the key geometric characteristics of the starter block. As a result, some researchers refer to the ratio of diameter-to-height, or the inverse, rather than specifying the optimal height or diameter directly. The optimal diameter-to-height ratio for the starter block is between 0.5 and 1 [4-7]. Furthermore, the geometry of the starter block affects the deviation of initial dendrites in the final single crystal. Increasing the height of the starter block decreased the final single crystal's deviation from the preferred crystal orientation [7,9,12,13]. Additionally, the effect of the starter block's geometry on this deviation is reported to be more significant than that of the withdrawal rate, which is a process parameter in Bridgman method affecting the solidification rate [12].

2. Materials and Methods

Table 1 presents the chemical composition of the CMSX-4 superalloy ingot used in this study, as determined by spark optical emission spectrometry (Spark-OES) using a quantometer at the Razi Applied Science Foundation laboratory. The alloy was made in a Vacuum Induction Melting (VIM) furnace. Directional solidification was facilitated at a mold withdrawal speed of 9 mm/min in a vertical Bridgman furnace (HRS).

Table1.
Chemical composition of the ingot used in the present study (wt.%).

Element	Ni	Al	Ti	Cr	Co	Mo	Ta	W	Re	Hf
Wt. %	Bal.	5.60	0.98	6.50	9.59	0.70	6.60	6.60	3.05	0.01

The melt refining was carried out in a Vacuum Arc Remelting (VAR) furnace. Table 2 provides the concentrations of trace elements (C, S, H, N, and O) measured after refining, as determined by gas analysis at the Razi Applied Science Foundation laboratory.

Table 2.
The amount of minor elements after refining the ingot in the VAR furnace.

Element	C	S	H	N	O
Amount	<0.001 wt.%	0.002 wt.%	2 ppm	5.1 ppm	13.5 ppm

Figure 1 is a schematic illustration of the mold components used in this study. The mold comprised a central rod for introducing the initial melt, surrounded by four cylindrical chambers.

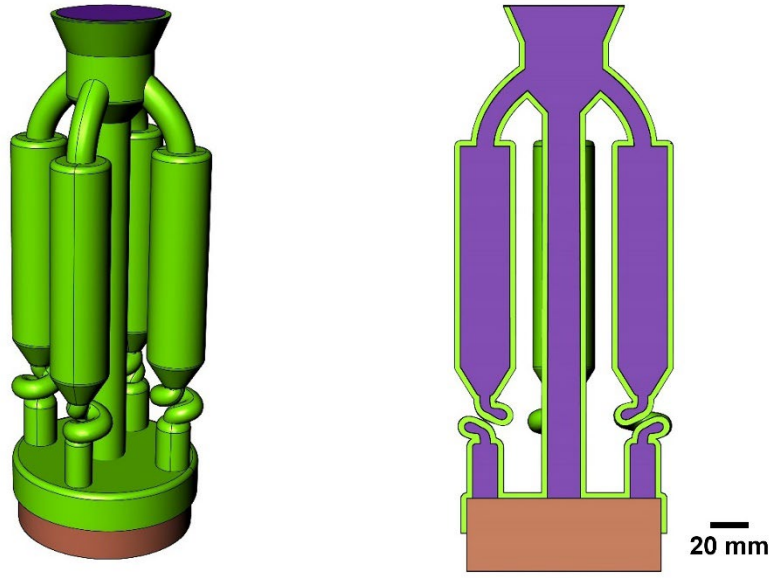


Fig. 1. Schematic diagram of the mold used in present study

Single crystal parts were cross-sectioned 70 mm above the chill plate, perpendicular to the cylinder axis. The samples were then prepared for Laue testing and hot-mounted using a Buehler mounting press. The resulting samples were examined using an X-ray crystal analyzer system by the Asenware LTD. The Laue test on the samples was conducted over a wavelength range of 0.07 to 0.2 nm and data analysis was performed using OrientExpress software.

Microstructural analysis was performed on longitudinal sections after cutting. Sample preparation included grinding with SiC abrasive papers (grit sizes 80, 120, 600, 800, 1000, and 2000), followed by polishing using a Buehler polishing apparatus. The samples were etched in a solution of copper chloride (5 grams), hydrochloric acid (100 mL), and ethanol (100 mL), by immersing for 1 minute. Microstructural examination was carried out using an OLYMPUS DP 25 optical microscope. The measurements of primary and secondary dendrite arm spacing were performed by counting dendrites with Image-J software.

The average primary and secondary dendrite arm spacing was determined by analyzing multiple micrographs (n = 5) taken at 50× magnification. Measurements were performed on a defined field of view area of 5,753,000 μm² using ImageJ software, based on Equations 1 and 2.

$$\lambda_1 = \sqrt{\frac{A}{N}} \quad (1)\ [15]$$

$$\lambda_2 = \frac{L}{N' - 1} \quad (2)\ [16]$$

The variables A, N, L, and N' in Equations 1 and 2 are explained in Figure 2.

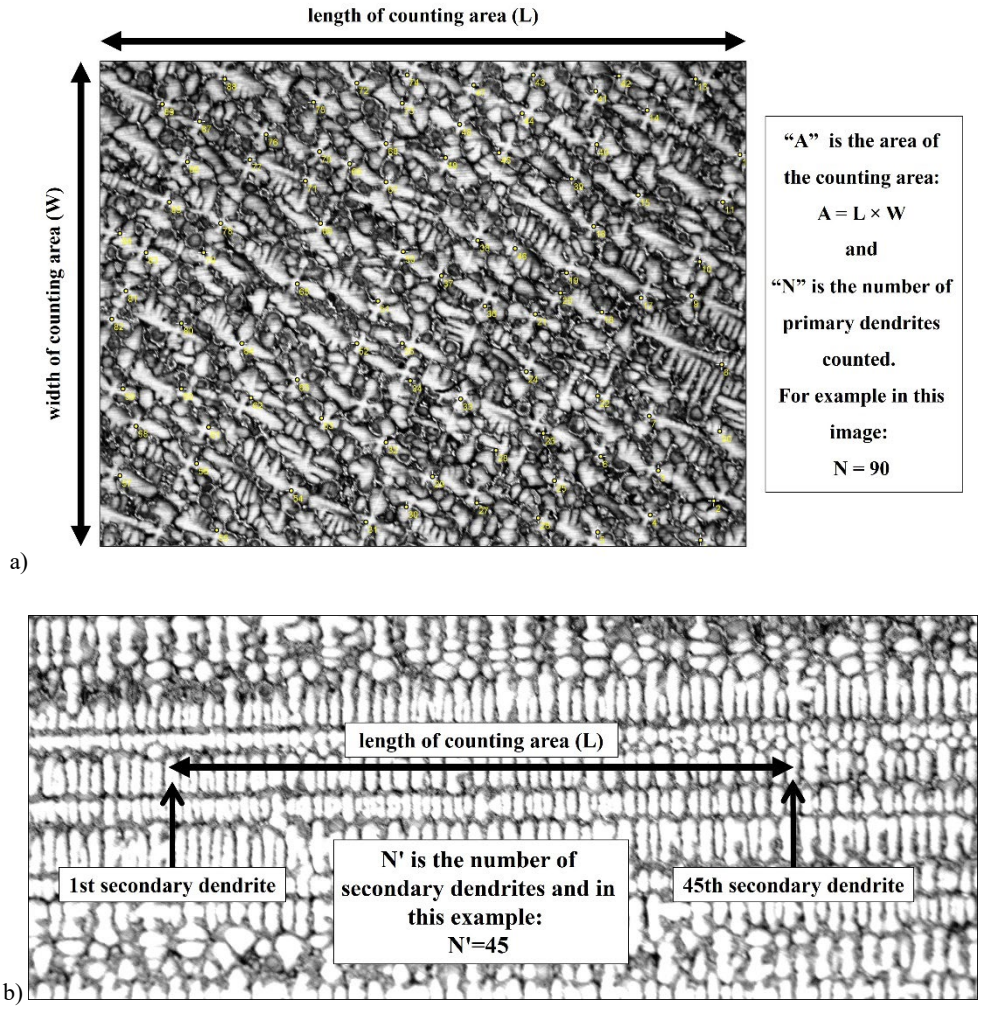


Fig. 2. Definition of variables in Equations a) 1 and b) 2

Finite-element thermal modeling of the directional solidification process was carried out with the ProCAST software package. A CMSX-4 alloy model was adopted, and the necessary thermophysical quantities (thermal conductivity, density, specific heat, latent heat of fusion, and the solidus and liquidus temperatures) were retrieved directly from the built-in material database without modification.

The thermal environment was constructed so as to reproduce the actual Bridgman furnace behavior. Thus, the hot-zone boundary facing the sample was held at 1500 °C, whereas the chill plate was maintained at 20 °C. Radiative exchange was accounted for through surface emissivities of 0.85 on the graphite parts, 0.80 on the ceramic mold, 0.50 on the inner cold-zone surface, and 0.40 on the insulating layer.

Heat loss by convection and conduction across contacting components was described with heat transfer coefficients consistent with standard Bridgman practice. A coefficient of 20 W m^{-2} K^{-1} was assigned to the cooling medium–mold interface, while 5000 W m^{-2} K^{-1} was applied between the cooling medium and water. The contact resistance at the casting–chill plate interface was treated as temperature dependent, taking values from 196 W m^{-2} K^{-1} at 1200 °C up to 750 W m^{-2} K^{-1} at 1500 °C; in the same way, the casting–mold interfacial coefficient rose from 50 W m^{-2} K^{-1} at 500 °C to 750 W m^{-2} K^{-1} at 1500 °C. A withdrawal speed of 9 mm/min was imposed on the sample train, consistent with the growth velocity adopted in the experiments.

The complete assembly (the starter block, the spiral grain selector, and the cylindrical casting) was discretized with a uniform 1 mm element size (first-order tetrahedral elements**)**. To limit the computational burden, coarse 10 mm elements were used over the insulation and furnace walls. In agreement with the experimental parts, the ceramic mold wall was modeled with a thickness of 8 mm.

To evaluate the effects of the starter block D/H ratio and the distance from the chill plate on grain count, a two-way analysis of variance (two-way ANOVA) was performed. The D/H ratio at three levels (0.3, 0.5, and 0.7) and the distance from the chill plate at three levels (9, 14, and 21 mm) were considered as independent factors, while grain count per unit area was treated as the dependent variable. For each condition, six spatially separated image-based measurements were collected to characterize within-casting variability; these measurements were not independent casting

replicates. Statistical significance was evaluated at $p < 0.05$. The main effects of D/H ratio and distance from the chill plate, as well as their interaction effect, were examined. Where appropriate, Tukey's post hoc test was used for pairwise comparisons between groups. All statistical analyses were performed using Minitab.

3. Results and discussion

Figure 3 shows the images of the parts along with the grain selection system, after being separated from the central runner. The diameter-to-height ratios of the starter blocks in these parts were 0.3, 0.5 and 0.7. From the Laue tests (after cross-sectional cutting of the parts), all three parts were found to be single crystal. The degree of deviation from the preferred crystallographic orientation is presented in Table 3.

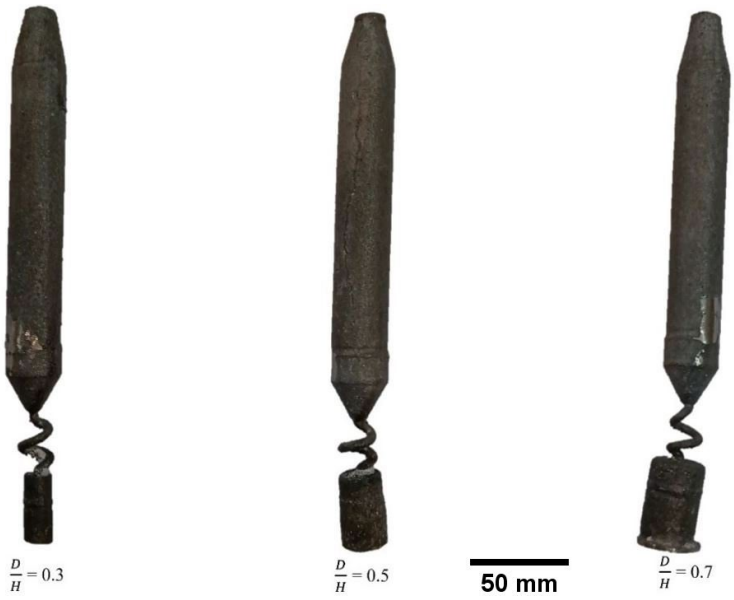


Fig. 3. Image of single crystal castings along with the grain selection system after separation from the central runner

Laue X-ray diffraction was performed at five distinct locations on each sample, and all measurements yielded the same crystallographic orientation within the examined cross-section. This result confirms orientation uniformity at the measurement plane. However, because only one casting was produced for each D/H condition due to experimental limitations, casting-to-casting reproducibility and statistical scatter of the misorientation angle could not be evaluated. The measured misorientation angles were 6.3°, 21.7°, and 3.3° for D/H ratios of 0.3, 0.5, and 0.7, respectively (Table 3). The D/H = 0.5 sample exhibited a considerably larger deviation, indicating a non-monotonic dependence. The lowest misorientation values were obtained for the castings with D/H ratios of 0.3 and 0.7. Both values were below the commonly accepted limit of 10° for single-crystal turbine components [2].

Table 3.
Misorientation angle from the preferred crystallographic orientation in single crystal castings based on the starter block's diameter-to-height ratio

Diameter-to-height ratio	0.3	0.5	0.7
Misorientation angle from the preferred crystallographic orientation	6.3˚	21.7˚	3.3˚

This non-monotonic behavior suggests that changing the D/H ratio alters the local solidification conditions within the starter block, rather than leading to a simple monotonic improvement in grain selection. Numerical simulation of solid-fraction evolution during mold withdrawal (Figure 4) indicated that, for the D/H = 0.3 condition, part of the melt remained unsolidified after the starter block passed the furnace heat baffle. This observation suggests that the position of the solidification front relative to the furnace thermal field was sensitive to starter-block geometry.

For the D/H = 0.5 condition, the smaller lag of the solidification front relative to the D/H = 0.3 case, together with the larger lateral surface area, may have increased the contribution of sidewall cooling after the starter block entered the colder zone. Under such transient thermal conditions, the solid-liquid interface may become more curved and less stable, which could facilitate the survival and competitive growth of grains with larger deviations from the preferred [001] direction. This mechanism is proposed as a

plausible explanation for the relatively high misorientation measured in the D/H = 0.5 sample.

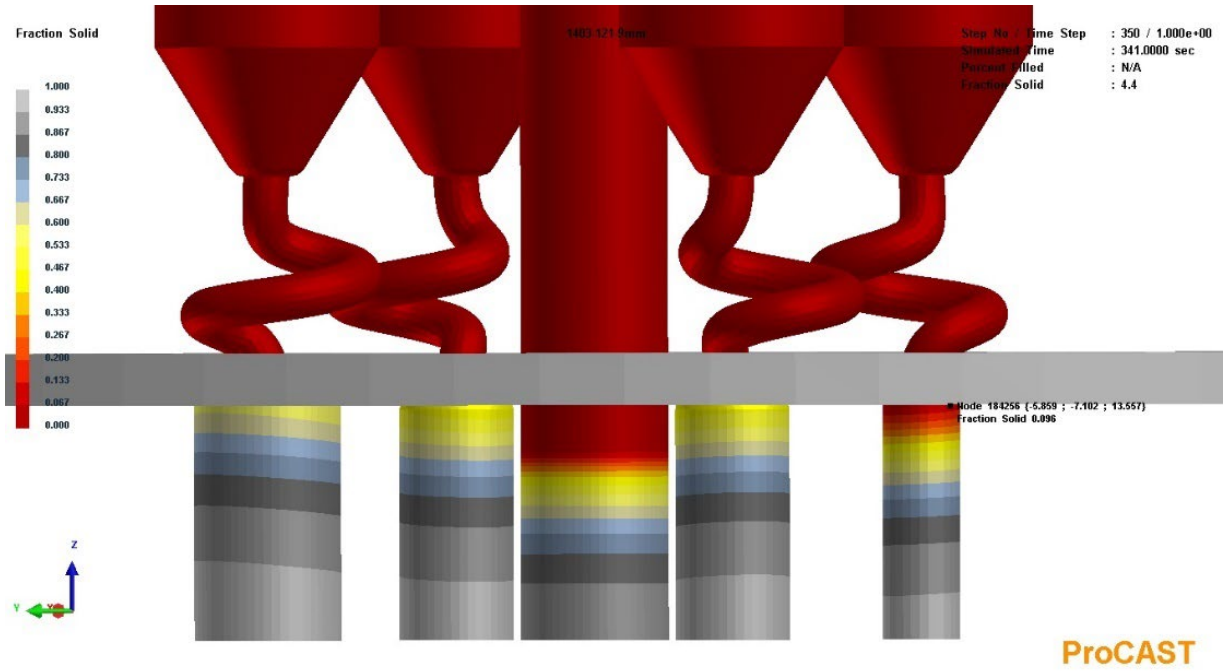


Fig. 4. ProCAST simulation of the solid fraction evolution during solidification in the starter-block region of cast single-crystal components at a withdrawal rate of 9 mm/min

For the D/H = 0.3 starter block, the smaller melt volume reduced the amount of heat that had to be removed from the starter region. As a result, axial heat extraction through the starter base and the copper chill plate likely remained the dominant heat-flow path. Although the simulation indicates that part of the melt was still unsolidified after passing the heat baffle, the limited melt volume appears to have helped maintain comparatively stable growth conditions, which is consistent with the relatively low misorientation measured for this sample.

In the D/H = 0.5 condition, the larger melt volume relative to D/H = 0.3 may have increased the thermal load in the starter region, making the solidification behavior more sensitive to lateral heat extraction after entering the colder zone. This condition could promote curvature of the solid-liquid interface and disturb the local growth direction of the primary dendrites. Because dendrite selection in single-crystal superalloys depends strongly on the local thermal field and crystallographic growth competition, such interface instability may contribute to the larger [001] misorientation observed in this sample.

For the D/H = 0.7 starter block, despite the larger melt volume, the larger cross-sectional area likely allowed a greater initial population of competing grains to form at the chill interface. This may increase the probability that grains with orientations closer to the preferred [001] direction participate in the competitive growth process and eventually reach the selector entrance. In addition, the simulation suggests that the solidification front remained closer to the heat baffle than in the D/H = 0.3 case, indicating relatively more favorable thermal conditions. These factors may explain the lower misorientation measured for the D/H = 0.7 sample.

As shown in the etched longitudinal sections (Figure 5), stray grains were observed in the castings with D/H ratios of 0.3 and 0.5, whereas no such grains were identified in the D/H = 0.7 sample. These stray grains were located outside the specific cross-sectional plane used for the Laue measurement at 70 mm above the chill plate; therefore, they were not reflected in the reported Laue misorientation values.

Under ideal and steady Bridgman conditions, the solid-liquid interface is expected to remain approximately stationary relative to the furnace hot zone and heat baffle while the mold is withdrawn downward. However, at the withdrawal rate used in this study (9 mm/min), the simulation suggests that the interface could not remain fully stabilized near the heat baffle and instead advanced into the colder region of the furnace. Such a shift may increase lateral heat extraction through the mold walls (sidewall cooling), distort the local thermal field, and generate curved isotherms together with a non-planar solid-liquid interface. The associated reduction in the effective thermal gradient may also increase the susceptibility to wall nucleation and stray-grain formation.

It should be noted that such nucleation conditions may occur in all samples once the interface enters the colder zone; nevertheless, the survival and growth of wall-nucleated grains strongly depend on the local dendrite alignment and competitive growth. In the D/H = 0.7 sample, where the measured misorientation was the smallest (3.3°), the primary dendrites were more closely aligned with the withdrawal axis. This alignment likely improved dendrite packing near the mold wall and reduced the available space for the survival of wall-nucleated grains. As a result, any incipient stray grains may have been suppressed by competitive overgrowth, which is

consistent with the absence of observable stray grains in this sample.

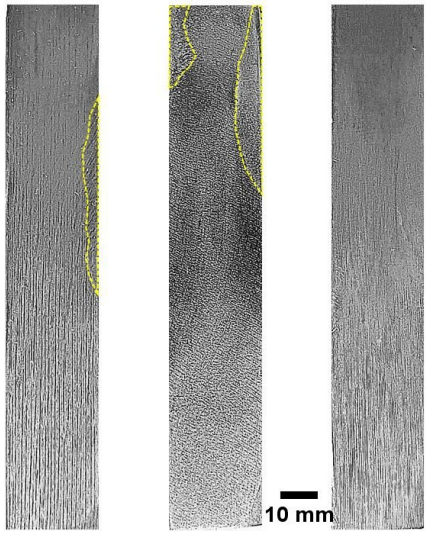


Fig. 5. Macroscopic image of etched longitudinal sections of single crystal castings with starter block diameter-to-height ratios of a) 0.3, b) 0.5, and c) 0.7, showing stray grains highlighted by dashed regions.

To further elucidate the thermal conditions prompting this behavior, numerical simulation of the temperature gradient during directional solidification was performed as shown in Figure 6. The simulation results indicate that, although the nominal thermal condition of the process corresponded to an overall furnace-scale gradient of approximately 13 °C/mm, the local thermal gradient in the upper cylindrical region of the casting decreased markedly as the solidification front advanced beyond the heat baffle. In these locally disturbed regions, the simulated gradient dropped to much lower values, reaching below 10 K/cm in some zones. This marked local reduction in thermal gradient may increase the susceptibility to constitutional undercooling and heterogeneous nucleation of stray grains along the mold wall. However, the physical survival and growth of these nucleated grains are governed by the crystallographic orientation and packing density of the primary dendrites.

In the D/H = 0.7 sample, the low measured misorientation (3.3°) was associated with primary dendrites that were more closely aligned with the withdrawal axis. This alignment may have improved dendrite packing near the mold interface and reduced the space available for wall-nucleated grains. The absence of observable stray grains in this sample is therefore consistent with their possible suppression by competitive overgrowth. Conversely, in the samples with larger misorientations (D/H = 0.3 and especially D/H = 0.5), the tilted growth of the primary dendrites may generate locally divergent regions near the mold wall. These relatively open zones can reduce dendrite impingement and provide more favorable conditions for the survival and growth of wall-nucleated stray grains in the upper part of the casting.

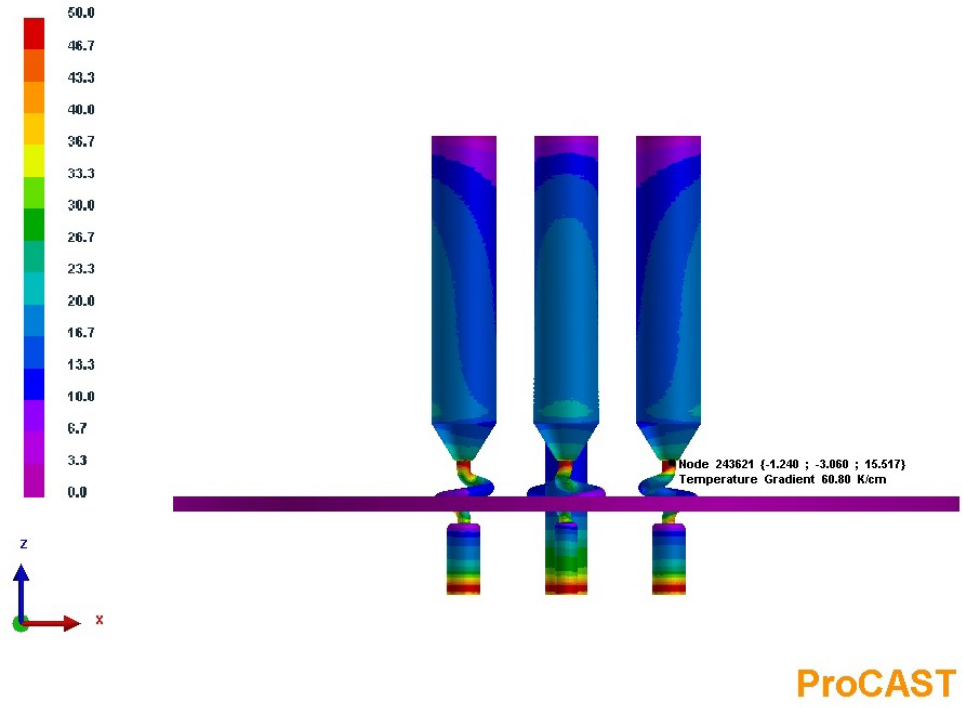


Fig. 6. ProCAST numerical simulation results showing the temperature gradient (G) distribution during the directional solidification of CMSX-4 castings with different starter block D/H ratios

Figure 7 shows the microstructure of the stray grain region in the single crystal part with diameter-to-height ratio of 0.5. The morphology and location of the stray-grain region adjacent to the mold wall are consistent with wall-associated heterogeneous nucleation. Additionally, the larger deviation of the primary dendrites from the preferred crystallographic orientation and the withdrawal axis may have reduced dendrite packing near the mold wall. This could have created a locally open region that facilitated the survival and growth of stray grains at the mold interface. Because the withdrawal axis is perpendicular to the chill plate, any deviation from the preferred crystallographic orientation (typically [001]) results in the primary dendrites being tilted relative to the mold axis. As a consequence, dendrite growth converged toward the mold wall on one side and diverged on the opposite side, thereby contributing to an asymmetric local solidification front. The misorientation of the primary dendrites may also have reduced dendrite impingement near one side of the mold wall, thereby creating a locally open region. This may have led to local undercooling and provided favorable conditions for the heterogeneous nucleation of stray grains.

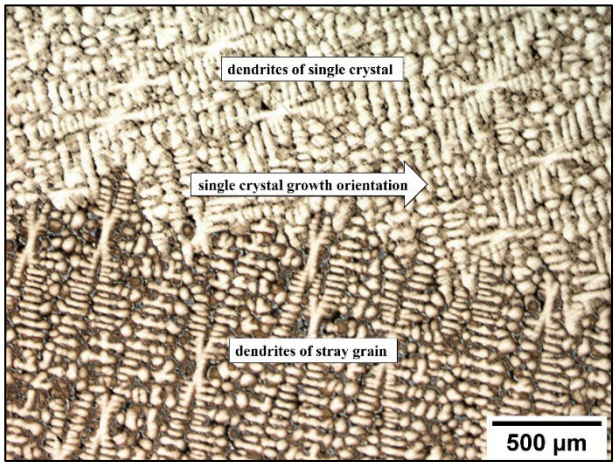


Fig. 7. Optical microscope image of the stray grain region in single crystal casting with starter block diameter-to-height ratio of 0.5.

Figure 8 shows the microstructure of a part with a diameter-to-height ratio of 0.5, which is representative of the microstructure of similar parts. Primary dendrites as well as secondary and tertiary dendrite arms are shown in this figure along with eutectic areas, coarse γ' phase and interdendritic porosities.

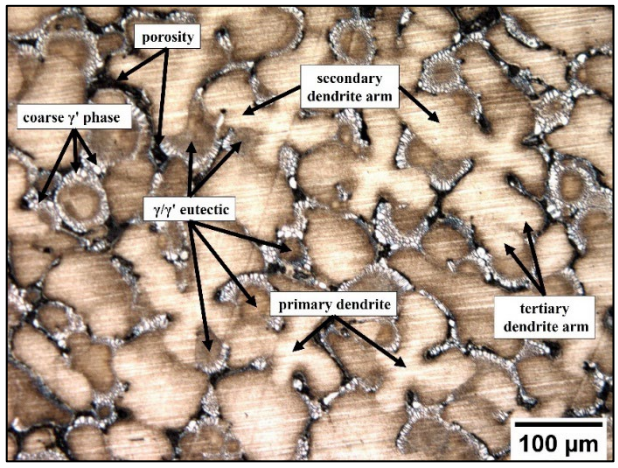


Fig. 8. Optical microscope image of the cross-section of the single crystal casting with a starter block diameter-to-height ratio of 0.5.

The interdendritic area at higher magnification is shown in Figure 9. Eutectic pools, which were formed at the final stage of solidification in interdendritic areas, contained coarse γ' phase and γ/γ' eutectic. These segregated regions must be reduced or eliminated through high-temperature diffusion during heat treatment, as one of the main purposes of this process is to homogenize the microstructure. Therefore, a lower amount of eutectic reduces the required heat treatment effort and overall production cost.

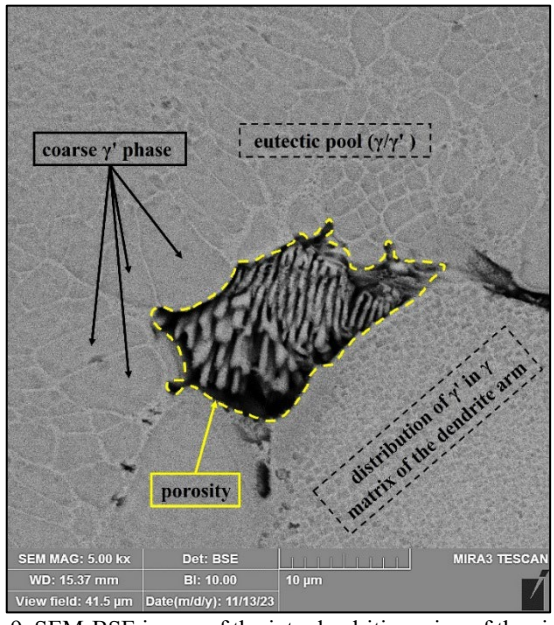


Fig. 9. SEM-BSE image of the interdendritic region of the single crystal casting with a starter block diameter-to-height ratio of 0.5, taken at a magnification of 5000×

Figure 10 presents the microstructure of the cross-sectional views of the single crystal parts. Figure 10 (a) and Figure 10 (c) in differ in color from Figure 10 (b) due to the greater deviation of the

primary dendrite arms from the preferred crystallographic orientation in Figure 10 (b). Tertiary dendrite arms were observed throughout the images in Figure 10, occupying the interdendritic spaces between secondary dendrite arms. Specifically, the primary dendrites that passed through the spiral grain selector should have covered the entire mold space upon entering. This objective was achieved by the formation of secondary and tertiary dendrite arms.

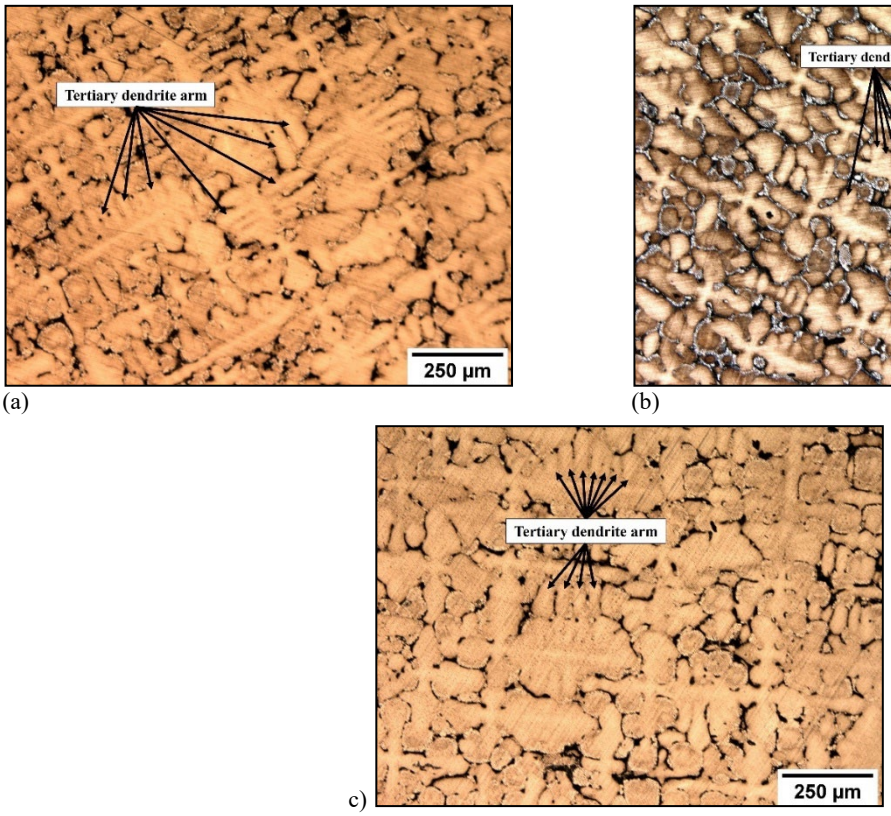


Fig. 10. Optical microscope images of the cross-sections of single crystal samples with starter block diameter-to-height ratios of a) 0.3, b) 0.5, and c) 0.7

Figure 11 shows the average primary dendrite arm spacing calculated using Equation 1. The average PDAS values for the castings with D/H ratios of 0.3, 0.5, and 0.7 were 226.4 (+17.6/−20.4) µm, 232.4 (+20.6/−9.4) µm, and 241.6 (+23.4/−14.6) µm, respectively. The asymmetric ranges indicate the differences between the mean and the observed maximum and minimum values. Although the mean PDAS increased slightly with increasing D/H ratio, the observed ranges overlapped substantially. Therefore, the present measurements do not provide sufficient evidence for a systematic effect of D/H ratio on PDAS.

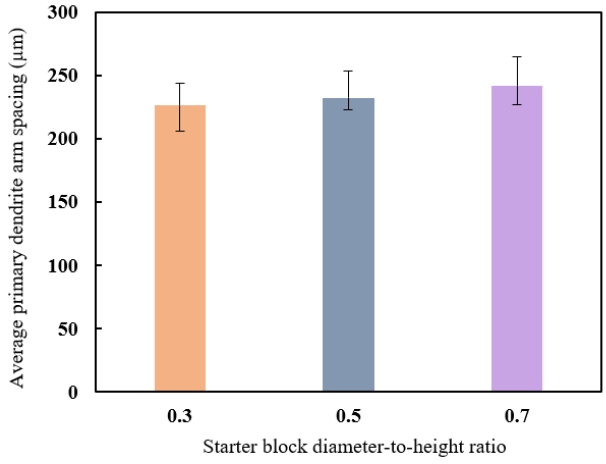


Fig. 11. Average primary dendrite arm spacing in single crystal castings with starter block diameter-to-height ratios of 0.3, 0.5, and 0.7

Figures 12 and 13 show the microstructures of the longitudinal sections of the single crystal parts with diameter-to-height ratios of 0.3 and 0.5, respectively. In the sample with a ratio of 0.3, the primary dendrites were nearly aligned with the part axis and withdrawal direction. In contrast, the sample with a ratio of 0.5 showed a noticeable misalignment between the primary dendrite growth direction and the part axis.

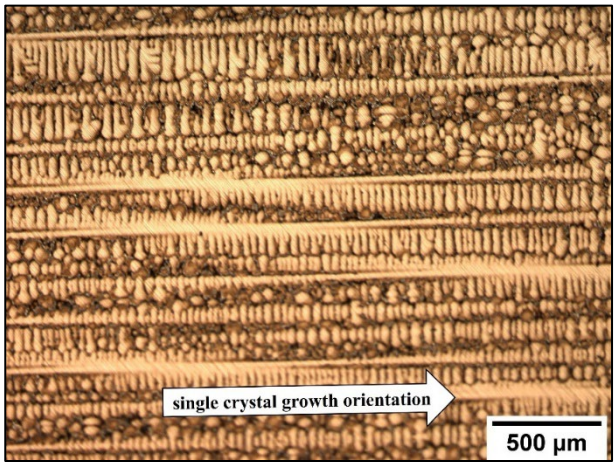


Fig. 12. Optical microscope image of the longitudinal section of single crystal part with starter block diameter-to-height ratio of 0.3

In contrast, Figure 13 shows that the primary dendrites in the single crystal part with a diameter-to-height ratio of 0.5 intersected the cutting plane and were tilted relative to the part's axis. The secondary dendrite arm spacing was calculated from the longitudinal images of the single crystal sections using Equation 2.

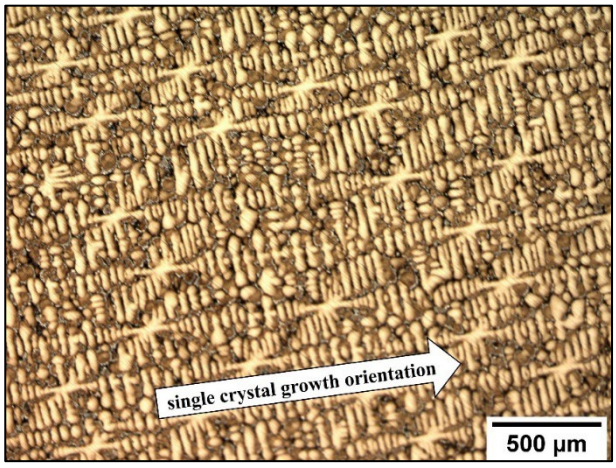


Fig. 13. Optical microscope image of the longitudinal section of single crystal part with starter block diameter-to-height ratio of 0.5

According to Figure 14, the average secondary dendrite arm spacing values in the single-crystal castings with D/H ratios of 0.3, 0.5, and 0.7 were 41.3 (+6.9/−6.1) µm, 36.7 (+4.6/−6.5) µm, and 39.3 (+5.8/−3.7) µm, respectively. The asymmetric ranges represent the differences between the mean and the observed maximum and minimum values. The measured ranges overlapped substantially, and no monotonic variation in SDAS with D/H ratio was observed. Therefore, within the resolution and spatial sampling of the present measurements, the data do not provide evidence of a systematic relationship between the starter-block D/H ratio and SDAS. Similarly, no consistent association between SDAS and the measured crystallographic misorientation was identified.

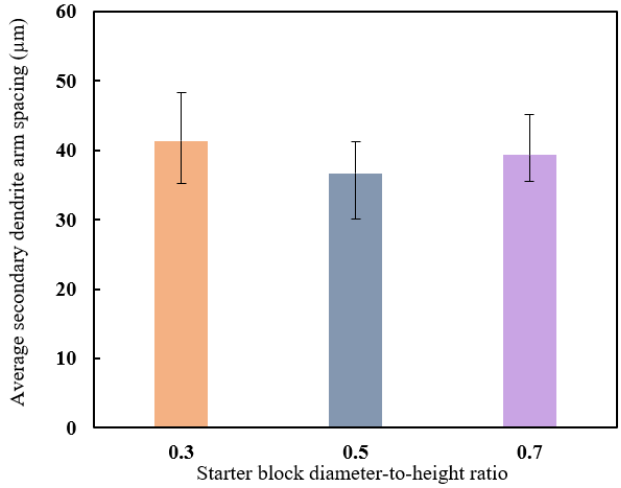


Fig. 14. Average secondary dendrite arm spacing in single crystal castings with diameter-to-height ratios of 0.3, 0.5, and 0.7

Based on the above findings, no statistically conclusive relationship was observed between the diameter-to-height ratio of the starter block and the primary (λ_1) and secondary (λ_2) dendrite arm spacing in the single crystal parts. Nevertheless, the starter block geometry may affect local solidification conditions and, consequently, the morphology and distribution of γ' precipitates within the primary dendrite cores.

The effect of the starter block diameter-to-height ratio on the γ' strengthening precipitates in the primary dendrite cores is shown in Figure 15.

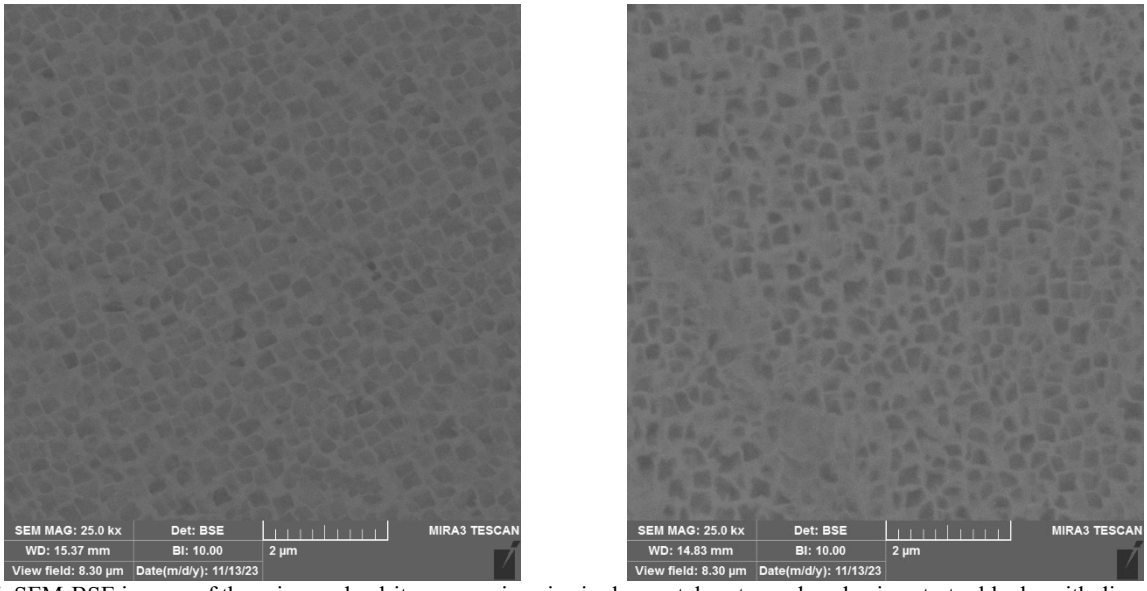


Fig. 15. SEM-BSE images of the primary dendrite core regions in single-crystal parts produced using starter blocks with diameter-to-height (D/H) ratios of (a) 0.3 and (b) 0.5

To provide a descriptive comparison of the γ′ precipitate morphology, the SEM-BSE micrographs obtained from the primary dendrite cores of the specimens with D/H ratios of 0.3 and 0.5 were contrast-enhanced and binarized using the same ImageJ processing procedure. The segmented bright γ′-related regions exhibited comparable area fractions of 61.872% and 62.433% for D/H = 0.3 and D/H = 0.5, respectively. Similarly, only minor differences were observed in the shape descriptors: circularity increased from 0.657 to 0.676, solidity increased from 0.853 to 0.873, and the aspect ratio changed from 1.39 to 1.41 as the D/H ratio increased from 0.3 to 0.5. However, the number of segmented γ′-related features decreased from 637 for D/H = 0.3 to 599 for D/H = 0.5. Considering the nearly identical area fractions, this difference indicates a relatively coarser or more interconnected appearance of the γ′-related regions at D/H = 0.5. Overall, the image-analysis results indicate broadly similar γ′ area fractions and shape characteristics for the two starter-block geometries. These observations are therefore presented as descriptive indicators of local γ′ morphology rather than statistically conclusive evidence of a direct effect of the starter-block D/H ratio.

Since the γ′-related regions showed comparable area fractions and only minor differences in the extracted shape parameters, the effect of starter-block geometry on the final crystallographic quality was further examined through competitive grain growth in different sections of the starter blocks. For this purpose, cross-sections were prepared at 9, 14, and 21 mm above the chill plate of the Bridgman furnace, as shown in Figure 16.

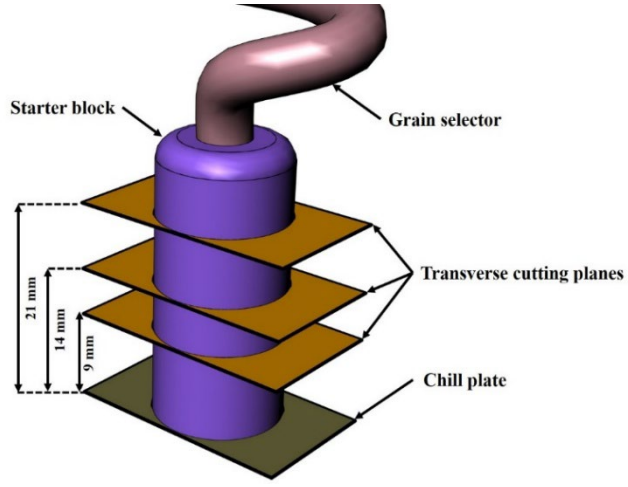


Fig. 16. Schematic illustration of the cross-section of the starter block at different distances from the chill plate

The microstructures of the cross-sections of starter blocks with different diameter-to-height ratios, based on the cuts shown in Figure 16, are presented in Figure 17. In all three starter blocks, as the distance from the chill plate increased, competitive grain growth led to the elimination of some grains, resulting in a decreased grain count per unit area in the region closer to the grain selector. Additionally, the removal of some grains during competitive growth created space for the dominant grain, leading to the development of secondary and tertiary dendrite arms.

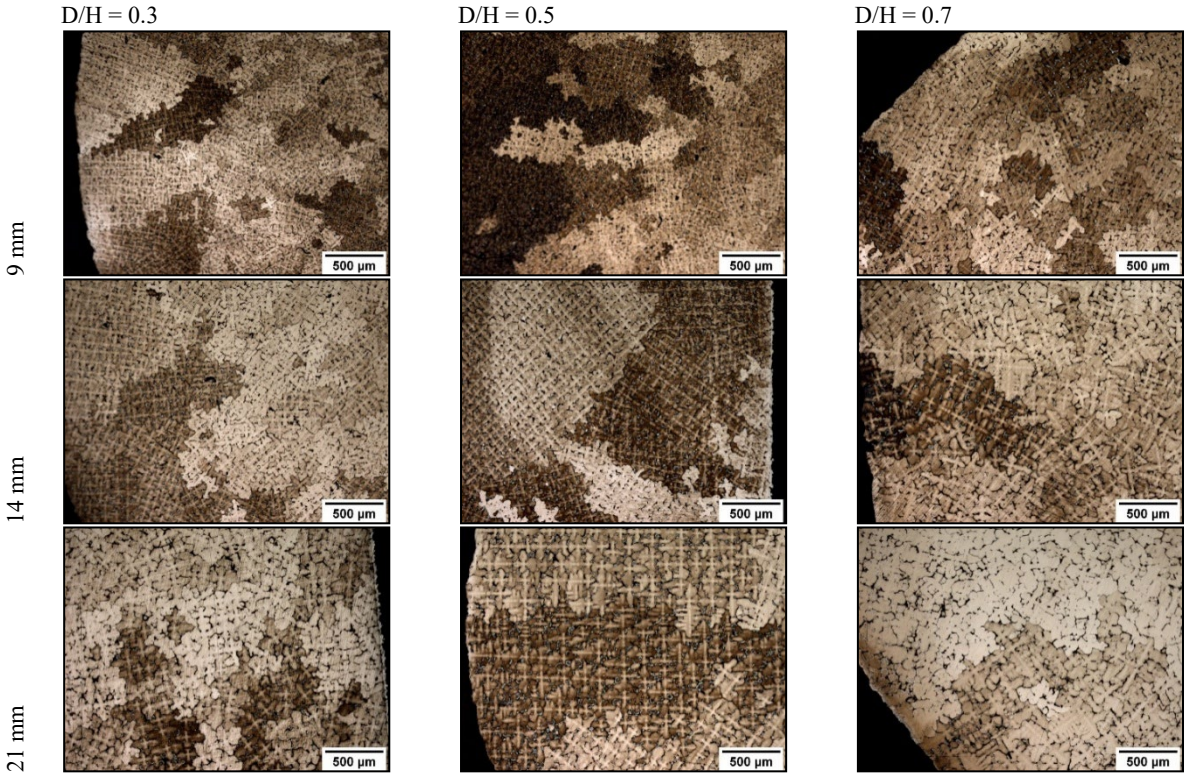


Fig. 17. Optical microscope images of cross-sections of starter blocks with different diameter-to-height ratios at distances of 9, 14, and 21 mm from the chill plate

Figure 18 shows the grain count per unit area at distances of 9, 14, and 21 mm from the chill plate for starter blocks with D/H ratios of 0.3, 0.5, and 0.7. While all conditions exhibited relatively high grain counts at 9 mm, increasing the distance resulted in a general reduction for all D/H ratios, reflecting the progressive elimination of unfavorably oriented grains during competitive growth [7]. To quantify this trend, linear regression revealed negative slopes ranging from −7.37 to −10.17 (grains mm^{-2})/mm. A two-way ANOVA subsequently confirmed significant main effects of both D/H ratio ($F = 8.53$, $p < 0.001$) and distance ($F = 62.00$, $p < 0.001$). Notably, the interaction was not statistically significant ($F = 0.89$, $p = 0.475$), suggesting that while D/H influences absolute grain density, it does not fundamentally alter the distance-dependent grain selection process trend, as visually supported by the broadly similar negative slopes in Figure 18.

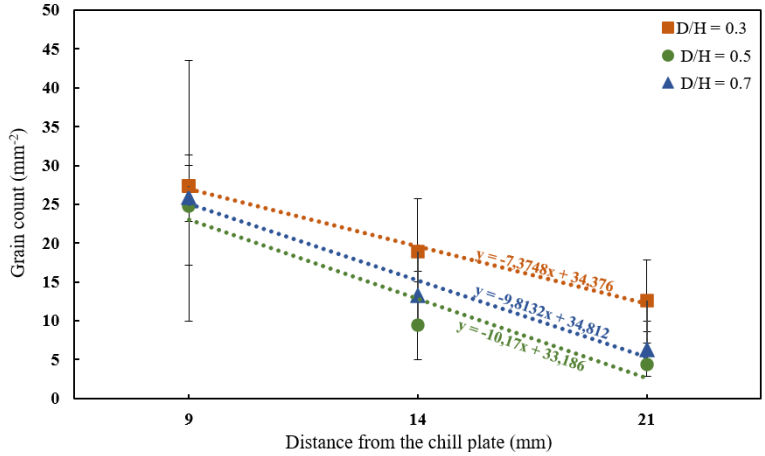


Fig. 18. Grain count per unit area as a function of distance from the chill plate for starter blocks with D/H ratios of 0.3, 0.5, and 0.7. The symbols represent the mean grain count, the error bars indicate the observed minimum-to-maximum range from six spatially separate measurements, and the dotted lines represent linear regression fits for the respective D/H ratios

Figure 19 shows the microstructure of the cross-section of starter block with diameter-to-height ratio of 0.7 in the region near the grain selector. The image shows the development of tertiary dendrite arms, which is a result of the reduction in the number of grains and the filling of the voids by the dominant grains.

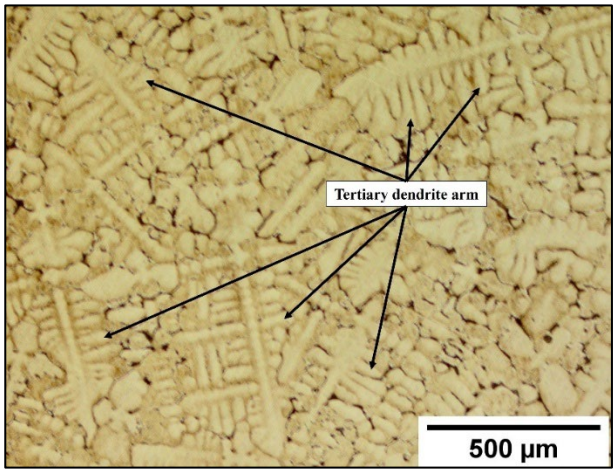


Fig. 19. Optical microscope image of the cross-section of starter block with diameter-to-height ratios of 0.7 at a distance of 30 mm from the chill plate

Figure 20 illustrates the calculated average primary dendrite arm spacing as a function of distance from the chill plate for all three diameter-to-height ratios of the starter block. Increased diameter-to-height ratio of the starter block generally led to increased primary dendrite arm spacing at various distances from the chill plate. Although at a distance of 9 mm from the chill plate, the average primary dendrite arm spacing was similar for blocks with diameter-to-height ratios of 0.3 and 0.5, in the starter block with a diameter-to-height ratio of 0.7, the mean primary dendrite arm spacing was greater. Additionally, the grain count per unit area was substantially lower, suggesting more extensive grain elimination under this condition.

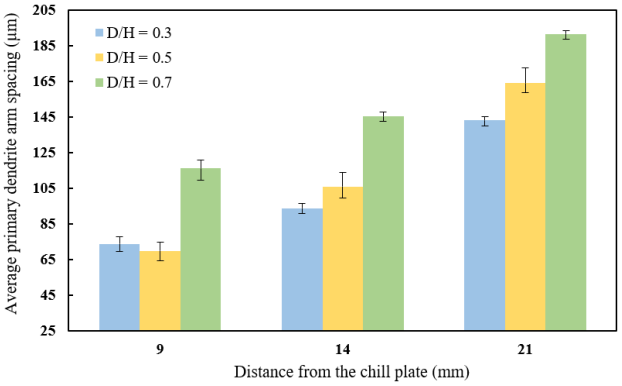


Fig. 20. Average primary dendrite arm spacing as a function of distance from the chill plate in starter blocks with different diameter-to-height ratios

Increasing the D/H ratio increased the molten-metal volume within the starter block and may therefore have modified the local cooling and solidification conditions. The more developed tertiary dendrite arms observed in the D/H = 0.7 starter block could be associated with the additional space created by progressive grain elimination; however, the present measurements are insufficient to attribute this observation directly to a reduction in cooling rate.

Figure 21 presents the average secondary dendrite arm spacing at a distance of 30 mm from the chill plate for starter blocks with different diameter-to-height ratios. The average secondary dendrite arm spacing at this distance shows only minor variation among the starter blocks with different diameter-to-height ratios.

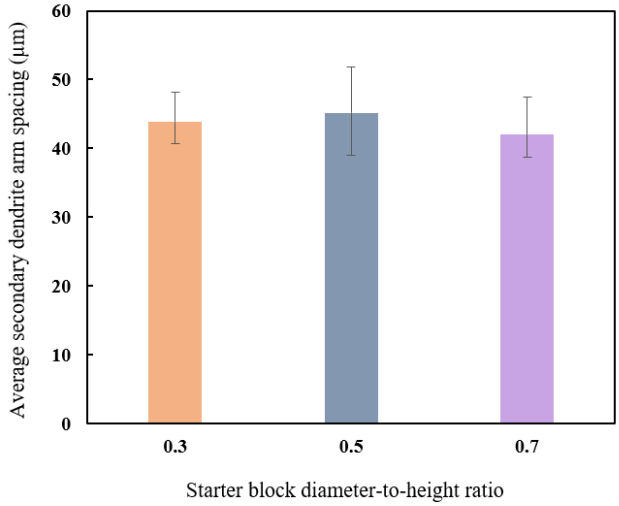


Fig. 21. Average secondary dendrite arm spacing as a function of distance from the chill plate in starter blocks with different diameter-to-height ratios

Overall, no systematic relationship was observed between the diameter-to-height ratio of the starter block and the average secondary dendrite arm spacing. Despite slight variations, the results largely overlapped. This suggests that the observed parameter may be more influenced by solidification conditions such as thermal gradient and withdrawal rate. However, as these factors were not directly measured or varied in this study, further investigation would be required to confirm this hypothesis.

4. Conclusions

This study investigated the influence of starter-block diameter-to-height (D/H) ratio on grain selection, crystallographic orientation, microstructural characteristics, and γ′ precipitate morphology in directionally solidified CMSX-4 single-crystal castings. Under the investigated processing conditions, all castings exhibited single-crystal growth within the examined Laue cross-sections; however, the measured crystallographic misorientation showed a non-monotonic dependence on starter-block geometry. The D/H ratios of 0.3, 0.5, and 0.7 resulted in misorientation angles of 6.3°, 21.7°, and 3.3°, respectively. Therefore, the D/H = 0.7 starter block provided the best crystallographic alignment among

the investigated conditions, whereas D/H = 0.5 produced the largest deviation from the preferred crystallographic orientation.

The combined experimental observations and ProCAST simulations indicate that starter-block geometry can modify the local thermal field and solidification-front behavior. In particular, advancement of the solidification front beyond the furnace heat baffle was associated with a marked local reduction in thermal gradient and increased susceptibility to sidewall cooling and wall-associated stray-grain nucleation. Stray grains were observed in the D/H = 0.3 and 0.5 castings, whereas no stray grains were detected in the D/H = 0.7 casting. The improved crystallographic alignment in the D/H = 0.7 condition may have promoted more effective dendrite packing and competitive overgrowth, thereby suppressing the survival of wall-nucleated grains.

Grain-count measurements at different distances from the chill plate confirmed progressive grain elimination during competitive growth. Both the D/H ratio and distance from the chill plate significantly affected the grain count, while their interaction was not statistically significant. Thus, the starter-block geometry influenced the absolute grain population but did not substantially alter the overall distance-dependent grain-selection trend within the studied range.

The average primary and secondary dendrite arm spacings showed overlapping measurement ranges, and no systematic relationship between D/H ratio and PDAS or SDAS was established. Likewise, image analysis of γ′-related regions in the primary dendrite cores showed comparable area fractions and only minor differences in shape descriptors for D/H = 0.3 and 0.5. Although the lower number of segmented γ′-related features for D/H = 0.5 (599 compared with 637 for D/H = 0.3) indicated a relatively coarser or more interconnected appearance, these observations were descriptive and do not demonstrate a conclusive direct effect of starter-block geometry on γ′ morphology.

Overall, the results demonstrate that the starter-block D/H ratio is an important geometrical parameter for controlling local thermal conditions, competitive grain growth, crystallographic alignment, and stray-grain susceptibility in CMSX-4 single-crystal castings. Among the investigated conditions, D/H = 0.7 provided the most favorable combination of low misorientation and the absence of observable stray grains. Nevertheless, because only one casting was produced for each D/H ratio, further experiments incorporating replicate castings and a broader range of starter-block geometries are required to establish statistical reproducibility and optimize the starter-block design.

References

[1] Wang, N., Liu, L., Gao, S., Zhao, X., Huang, T., Zhang, J. & Fu, H. (2014). Simulation of grain selection during single crystal casting of a Ni-base superalloy. *Journal of Alloys and Compounds*. 586, 220-229. https://doi.org/10.1016/j.jallcom.2013.10.036.

[2] Raza, M.H., Wasim, A., Hussain, S., Sajid, M. & Jahanzaib, M. (2019). Grain selection and crystal orientation in single-crystal casting: state of the art. *Crystal Research and Technology*. 54(2), 1800177, 1-9. https://doi.org/10.1002/crat.201800177.

[3] Meng, X., Lu, Q., Li, J., Jin, T., Sun, X., Zhang, J. & Hu, Z. (2012). Modes of grain selection in spiral selector during directional solidification of nickel-base superalloys. *Journal of Materials Science & Technology*. 28(3), 214-220. DOI: 10.1016/S1005-0302(12)60044-9.

[4] Wang, B., Zeng, L. & Li, J. (2022). A geometry optimization of spiral grain selector during directional solidification of nickel-based superalloy. *Crystal Research and Technology*. 57(9), 2100257, 1-8. https://doi.org/10.1002/crat.202100257.

[5] Carter, P., Cox, D.C., Gandin, C.A. & Reed, R.C. (2000). Process modelling of grain selection during the solidification of single crystal superalloy castings. *Materials Science and Engineering: A*. 280(2), 233-246. https://doi.org/10.1016/S0921-5093(99)00701-7.

[6] Sadeghi, F., Kermanpur, A. & Norouzi, E. (2018). Optimizing grain selection design in the single-crystal solidification of Ni-based superalloys. *Crystal Research and Technology*. 53(12), 1800108, 1-8. https://doi.org/10.1002/crat.201800108.

[7] Zhu, X., Wang, F., Wittenzellner, T., Zhang, S., Hemes, S. Mathes, M. & Bührig-Polaczek, A. (2019). Investigation of start block and corresponding influence for grain selection during casting of single-crystal superalloys. *Materials*. 12(10), 1717, 1-9. https://doi.org/10.3390/ma12101717.

[8] Pan, D., Xu, Q., Liu, B., Li. J., Yuan, H. & Jin, H. (2010). Modeling of grain selection during directional solidification of single crystal superalloy turbine blade castings. *JOM: The Journal of The Minerals, Metals & Materials Society.* 62(5), 30-34. https://doi.org/10.1007/s11837-010-0074-y.

[9] Gao, S. F., Liu, L., Zhao, X. B., Huang, T. W., Zhang, J. & Fu, H. Z. (2011). Effects of spiral geometries on grain selection during casting of single crystal superalloys. *Materials Science and Technology*. 27(12), 1783-1787. https://doi.org/10.1179/1743284711Y.0000000074.

[10] Jiang, L.W., Li, S.S., Wu, M.L. & Han, Y.F. (2013). Grain competition mechanism of a Ni3Al-based single crystal superalloy IC6SX. *Materials Science Forum.* 747, 797-803. https://doi.org/10.4028/www.scientific.net/MSF.747-748.797.

[11] Szeliga, D., Kubiak, K., Burbelko, A., Motyka, M. & Sieniawski, J. (2014). Modeling of directional solidification of columnar grain structure in CMSX-4 nickel-based superalloy castings. *Journal of Materials Engineering and Performance*. 23(3), 1088-1095. https://doi.org/10.1007/s11665-013-0820-8.

[12] Rezaei, M., Kermanpur, A. & Sadeghi, F. (2018). Effects of withdrawal rate and starter block size on crystal orientation of a single crystal Ni-based superalloy. *Journal of Crystal Growth*. 485, 19-27. https://doi.org/10.1016/j.jcrysgro.2017.12.040.

[13] Seo, S.M., Kim, I.S., Lee, J.H., Jo, C.Y., Miyahara, H. & Ogi, K. (2009). Grain structure and texture evolutions during single crystal casting of the Ni-base superalloy CMSX-4. *Metals and Materials International*. 15(3), 391-398. https://doi.org/10.1007/s12540-009-0391-2.

[14] Yan, Y.H., Liu, J., Jia, Z.H., Qiu, S., Guo, Z., Liu, K. & Xu, L. (2017). Simulation and experimental studies on grain selection behavior of DD5 single crystal superalloy. *Materials Science Forum.* 878:42-50.

[15] Kostić, S., Golubović, A. & Valčić, A. (2009). Primary and secondary dendrite spacing of Ni-based superalloy single crystals. *Journal of the Serbian Chemical Society*. 74(1), 61-69. DOI: 10.2298/JSC0901061K.

[16] Vandersluis, E. & Ravindran, C. (2017). Comparison of measurement methods for secondary dendrite arm spacing. *Metallography Microstructure and Analysis*. 6(1), 89-94. https://doi.org/10.1007/s13632-016-0331-8.